Journal of
Materials Chemistry C

Flexible crystalline β-Ga2O3 solar-blind photodetectors

Journal:	*Journal of Materials Chemistry C*
Manuscript ID	TC-ART-08-2020-003740.R1
Article Type:	Paper
Date Submitted by the Author:	30-Aug-2020
Complete List of Authors:	Lai, Junyu; University at Buffalo - The State University of New York, Materials Design and Innovation Hasan, Md ; University at Buffalo - The State University of New York, Materials Design and Innovation Swinnich, Edward; University at Buffalo - The State University of New York, Materials Design and Innovation Tang, Zhao; University at Buffalo - The State University of New York, Physics Shin, Sangho; Nanyang Technological University, EEE Kim, Munho; Nanyang Technological University, EEE Zhang, Peihong; University at Buffalo - The State University of New York, Physics Seo, Jung-Hun; University at Buffalo - The State University of New York, Materials Design and Innovation

ARTICLE

Flexible Crystalline β-Ga_2O_3 Solar-blind Photodetectors

Junyu Lai[a], Md Nazmul Hasan[a], Edward Swinnich[a], Zhao Tang[b], Sang-Ho Shin[c], Munho Kim[c], Peihong Zhang[b], Jung-Hun Seo[a,*]

Received 00th January 20xx,
Accepted 00th January 20xx

DOI: 10.1039/x0xx00000x

This paper reports a demonstration of β-Ga_2O_3 nanomembrane (NM) based flexible photodetectors (PDs) and their optoelectrical properties under bending conditions. Flexible β-Ga_2O_3 NM PDs exhibited a reliable solar-blind photo-detection under bending conditions. Interestingly, a slight shifting in wavelength of the maximum solar-blind photo-current was observed under the bending condition. To investigate the reason for this peak shifting, optical properties of β-Ga_2O_3 NMs under different strain conditions were measured and revealed the changes in the refractive index, extinction coefficient and bandgap of strained β-Ga_2O_3 NMs due to the presence of nano-sized cracks in β-Ga_2O_3 NMs. A Multiphysics simulation and a density-functional theory calculation results for strained β-Ga_2O_3 NMs showed that the conduction band minimum and the valence band maximum states were shifted nearly linearly with the applied uniaxial strain which caused changes in optical properties in β-Ga_2O_3 NM. We also found that nano-gaps in β-Ga_2O_3 NM play a crucial role in enhancing photoresponsivity of β-Ga_2O_3 NM PD under bending conditions due to secondary light absorption by reflected light from nano-gap surfaces. Therefore, this research provides a viable route to realize high-performance flexible photodetectors which is one of the indispensable components in future flexible sensor systems.

Introduction

Wide bandgap (WBG) semiconductor-based solar-blind photodetectors (PDs) have attracted considerable attention as an emerging technology due to their unique spectral working region, which covers the deep ultra-violet (UV) range below 300 nm, significant potential in many military and commercial applications, such as ozone hole monitoring, deep space exploration, satellites, and secure data communication.[1-3] Among WBG semiconductors, beta-phase gallium oxide (β-Ga_2O_3) is considered a promising material candidate because it has superior UV photodetection performance due to its excellent electrical properties that are associated with a large bandgap, and intrinsically correspond to the solar-blind property.[4, 5] To date, several β-Ga_2O_3 based solar-blind PDs have demonstrated on a planar structure or with unique nanostructures for realizing solar-blind UV photodetection. For example, Kanika et al demonstrated a self-powered β-Ga_2O_3 thin film solar-blind PDs fabricated on Si substrate which exhibited a high on/off (I_{254nm}/I_{dark}) ratio of $>10^3$ and high responsivity of 96.13 AW^{-1}.[6] Zou et al. presented a deep UV PDs with an ultralow dark current (below the detection limit of 10^{-14} A), an extremely high I_{light}/I_{dark} ratio exceeding 10^6 with responsivity was as high as 851 AW^{-1} and fast response speed of <0.3s.[7] All of these studies show that β-Ga_2O_3 based PDs exhibit a promising on/off ratio, solar-blind properties, and photo responsivity that fulfill the demands of the typical rigid form of high-performance solar-blind photodetectors.[8] On the other hand, there is a wider spectrum of solar-blind PD based optoelectronic applications in which similar levels of UV detection and mechanical flexibility are simultaneously needed such as wearable UV monitor, flexible UV image sensor, and epidermal UV colorimetric dosimeter.[9-11] Therefore, the development of a freestanding and flexible form of β-Ga_2O_3, also called β-Ga_2O_3 nanomembranes (NMs) would directly benefit numerous future applications that have combined advantages of the rigid PDs such as high photoresponsivity and sensitivity in addition to the flexible ones such as good mechanical bendability and durability. In fact, flexible optoelectronics based on single crystalline semiconductor NMs, such as Si, III-V, zinc oxide (ZnO), gallium nitride (GaN), and silicon carbide (SiC) have been recently demonstrated but only covered in near-infrared and visible range due to their smaller bandgap[12-18], thus β-Ga_2O_3 NM-based flexible PDs will open up a new avenue in deep UV photodetection in a flexible format. However, although β-Ga_2O_3 NM based flexible PDs present a great potential for a myriad of applications, these PDs have not been demonstrated due to various technical challenges associated with a process such as a high-temperature metallization process and difficulty in creating and relocating separated β-Ga_2O_3. In 2014, a free-standing form of β-Ga_2O_3 NMs created from its' bulk substrate using a mechanical exfoliation method was developed by Prof. Jena's group at Cornell University and Prof. Ye's group at Purdue University

[a] Department of Materials Design and Innovation, University at Buffalo, The State University of New York, Buffalo, NY USA 14260
[b] Department of Physics, University at Buffalo, The State University of New York, Buffalo, NY USA 14260
[c] School of Electrical and Electronic Engineering, Nanyang Technological University, Singapore, Singapore 639798
*Email: junghuns@buffalo.edu (J.-H. Seo)
Electronic Supplementary Information (ESI) available: [details of any supplementary information available should be included here]. See DOI: 10.1039/x0xx00000x

after which several rigid types of β-Ga_2O_3 NMs based devices were demonstrated.[19-21] Recently, our group realized the first β-Ga_2O_3 NMs flexible high power switching devices using a micro-transfer printing method to place β-Ga_2O_3 NMs to desired places on a plastic substrate.[22]

In this paper, we report the first successful demonstration of β-Ga_2O_3 NM-based flexible solar-blind Schottky barrier type photodetectors using a micro-transfer printing technique. The flexible β-Ga_2O_3 NMs photodetectors exhibit excellent solar-blind property under the UV illumination. Interestingly, the solar-blind peak positions measured under flat and bending conditions were slightly shifted from 252 nm for a flat condition to 260 nm for the bending condition. To investigate the reason for the peak shifting, we performed a structural property analysis using atomic force microscopy (AFM) and characterized an optical property of β-Ga_2O_3 NMs which revealed slight changes in refractive index (n) and extinction coefficient (k) due to the presence of nano-sized cracks in β-Ga_2O_3 NMs. A multiphysics structural analysis and a density-functional theory (DFT) calculation were also performed to understand the optoelectrical behavior of β-Ga_2O_3 NM under the strain condition. This result provides a viable route in the realization of high performance flexible solar-blind photo-detection systems, which is one of the indispensable and important components in the upcoming internet of things era.

Results and discussion

Fig. 1(a) presents an illustration of the transfer printed β-Ga_2O_3 NM on a flexible polyimide (PI; Sigma Aldrich) substrate. The details of the fabrication process can be found in the supplementary Information (Fig. S1), but to be brief, the fabrication began with a mechanical cleaving of several large segments from bulk β-Ga_2O_3. The bulk β-Ga_2O_3 was grown by molecular beam epitaxy (by Novel crystal) and doped with Sn at 1×10^{18} cm^{-3} in the [201] direction. As shown in Fig. S1(a)(i), β-Ga_2O_3 bulk was cleaved along an angle of 77° due to its highly anisotropic monoclinic crystal structure. [22] β-Ga_2O_3 fakes were then created and ready to be exfoliated using a well-known micromechanical cleavage technique (also known as the "Scotch-tape" method). After this step, sub-micron thin β-Ga_2O_3 fakes were called β-Ga_2O_3 NMs. The crystal orientation of the cleaved surface became the [100] direction in β-Ga_2O_3 NMs. After exfoliation β-Ga_2O_3 NMs were obtained, we carefully transfer-printed them onto an adhesive (SU-8 2002; MicroChem) coated plastic substrate (PI, polyimide; Sigma Aldrich) by using an elastomeric stamp (polydimethylsiloxane, PDMS), followed by a curing process to permanently bond the β-Ga_2O_3 NMs onto the PI substrate as shown in Fig. 1(a). (Also shown in Fig. S1(a)(ii) – (v)). Fig. 1(b) and (c) present a three-dimensional and cross-sectional profiles of the transfer-printed β-Ga_2O_3 NM on the PI substrate captured using a surface profilometer (Filmetric Profilm3D). A thickness of transfer printed β-Ga_2O_3 NMs were measured to 370 nm. After completion of the transfer and bonding processes, a Ti/Au Ohmic metal stack (Ti/Au= 10/100 nm) and a Ti/Pt/Au Schottky metal stack (Ti/Pt/Au = 10/30/150 nm) were deposited to complete the fabrication of the device (Fig. S1(a)(vi)). Prior to Ohmic metal deposition, plasma treatment was carried out on β-Ga_2O_3 NMs by a BCl_3/Ar plasma treatment using a reactive ion etcher (RIE) to achieve ohmic contact and to avoid an additional high-temperature annealing process. Then, the sample was then ready for the electrical and optical characterization under different bending conditions. Fig. 1(d) illustrates the device

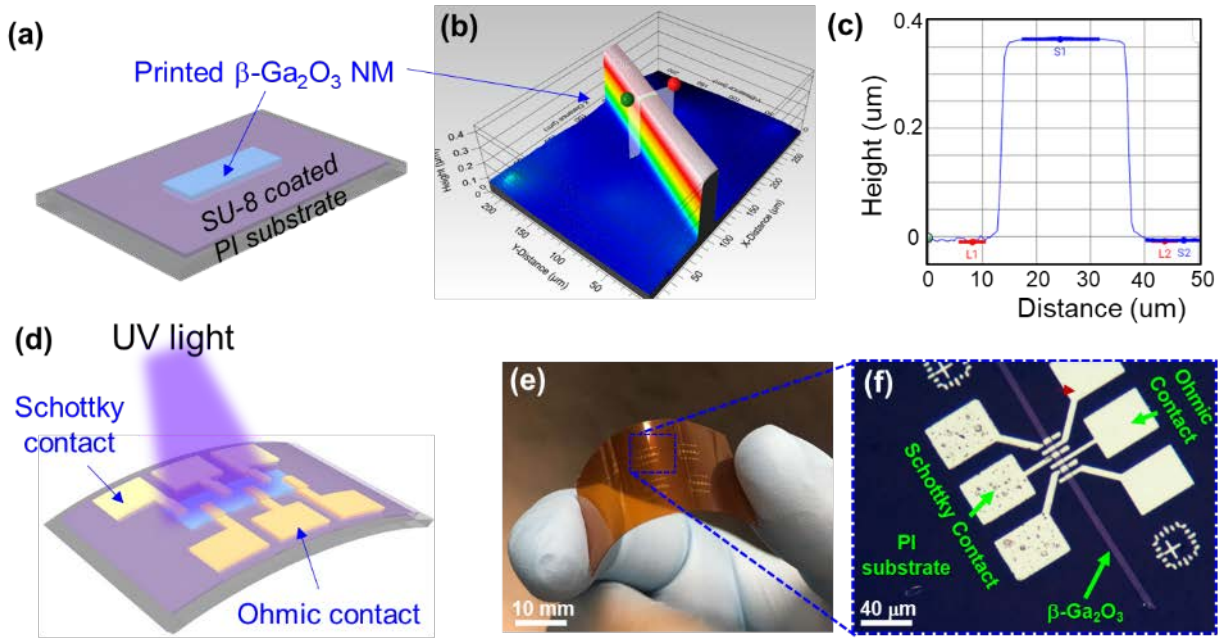

Figure 1. (a) An illustration of printed β-Ga_2O_3 NM on SU-8 coated PI substrate. **(b)** A three-dimensional morphology and **(c)** a cross-section of printed β-Ga_2O_3 NM on PI substrate. **(d)** an illustration of the β-Ga_2O_3 NM PD under the bending test. **(e)** a camera image of fabricated β-Ga_2O_3 NM PDs under bending condition. **(f)** a microscopic image of the finished β-Ga_2O_3 NM PDs.

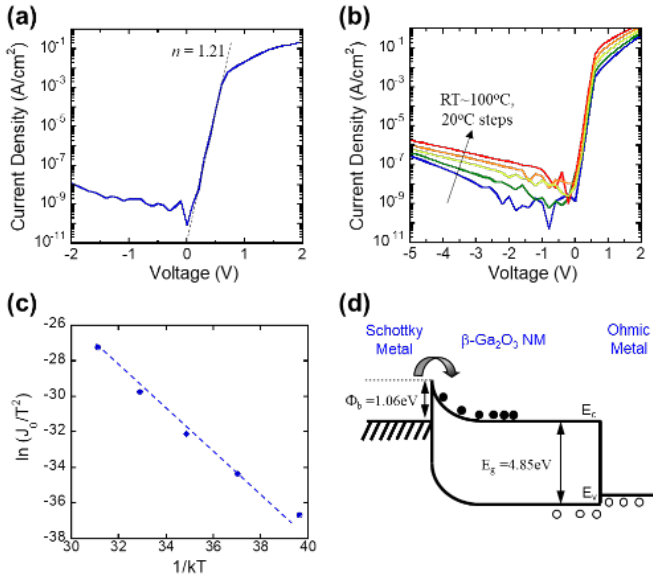

Figure 2. (a) J-V characteristics flexible β-Ga_2O_3 NM PDs at a flat condition. **(b)** Temperature-dependent J-V characteristics of flexible β-Ga_2O_3 NMs PDs at a flat condition. **(c)** Richardson's plot of β-Ga_2O_3 NM PDs at a flat condition. **(d)** A re-constructed band diagram of β-Ga_2O_3 NM PDs using measured parameters.

characterization under UV illumination and Fig. 1(e) and (f) show the camera image and microscopic image of as-fabricated β-Ga_2O_3 NM PDs under bending condition.

The electrical property of β-Ga_2O_3 NM PDs was measured using a Keithley 4200 semiconductor parameter analyzer. Fig. 2(a) shows the current density-voltage (J–V) characteristics of β-Ga_2O_3 NM PDs at a flat condition. The devices exhibited good rectifying behavior with an ideality factor (n) of 1.21 and an on/off ratio higher than 10^6, which are similar to the rigid version of the β-Ga_2O_3 NM PDs reported by others.[23] Fig. 2(b) shows the temperature-dependent J–V characterization of β-Ga_2O_3 NM PDs over a temperature ranged from 293 K (20 °C) to 373 K (100 °C). A stable rectifying behavior was observed at all temperatures. As the operating temperature increased, both forward and reverse current increased smoothly which can be explained by thermally generated carrier tunneling and the thermionic emission across the Schottky barrier.[24] To obtain a better understanding of the Schottky barrier height of the device, the Richardson's plot was used. Firstly, the J–V relationship for a metal-semiconductor diode, based on the thermal emission theory, can be expressed as[25]:

$$J = J_s\left\{\exp\left(\frac{qV}{nkT}\right) - 1\right\} \quad (1)$$

where J_s is the saturation current density that can be calculated from equation (2):

$$J_s = \frac{I_s}{A} = A^* \cdot T^2 \cdot \exp\left(-\frac{q\phi_b}{kT}\right) \quad (2)$$

where, A^* is the effective Richardson constant, the term ϕ_b is the Schottky barrier, q is the electron charge, V is the forward bias voltage, A is the effective diode area, k is the Boltzmann's constant, T is the temperature in Kelvin and n is the ideality

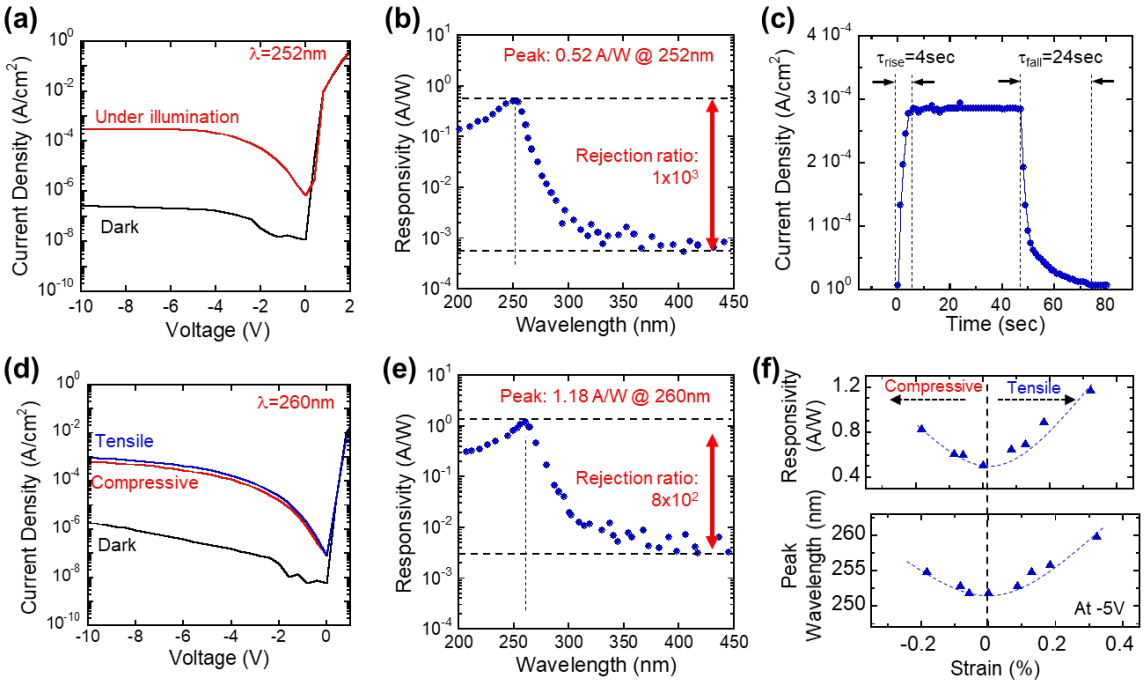

Figure 3. **(a)** J-V characteristics of β-Ga_2O_3 NM PDs under dark and 252 nm light illumination at flat condition. **(b)** Photoresponse spectrum of the β-Ga_2O_3 NM PDs under a flat condition at a voltage bias of -5 V. **(c)** Single response time for turned-on and turned-off states at -10 V. **(d)** J-V characteristics of β-Ga_2O_3 NM PDs under dark and 260 nm light illumination under bending condition. **(e)** Photoresponse spectrum of the β-Ga_2O_3 NM PDs under bending condition at a bias voltage of -5 V. **(f)** plot of peak photoresponsivity and peak wavelength with respect to strain.

Table 1. A comparison of our work with some of the representative flexible photodetectors based on other wide bandgap single-crystalline semiconductors.

Materials	Wavelength (nm)	Responsivity (AW^{-1})	Max. bending strain	Bandgap (eV)	Device Type	Substrate	Ref.
This work	253	1.18	0.35%	4.9	SBD	PI	
β-Ga_2O_3 NWs	254	0.71	8 mm (bending radius)	4.9	MSM	Glass fiber	4
β-Ga_2O_3 / graphene	254	29.8	NA	4.9	MSM	PET	30
α-Ga_2O_3 thin films	270	9.7	5 mm (bending radius)	4.8	MSM	muscovite	31
α-Ga_2O_3 thin films	254	43.99	30 cm (bending radius)	4.8	MSM	PET	32
GaN NWs/Graphene	365	98.04	3%	3.4	MSM	PET	33
InGaN/GaN quantum wells	370	0.096	NA	3.35	PN photodiode	Sapphire	34
ZnO NWs arrays/Ag NWs	365	4.16	3 mm (bending radius)	3.4	MSM	PET	35
ZnO NWs/PdS QDs	360	0.051	180^0C (bending angle)	3.4	MSM	PET	36
ZnO NWs	365	4.3	27 mm (bending radius)	3.3	MSM	PVC	37
SiC NWs	445	12.2	NA	2.9	MSM	PET	38
h-BN nanosheets	185	$5*10^{-5}$	10 mm (bending radius)	5.97	MSM	BN nano paper	39

factor. For the evaluation of the Schottky barrier height, Equation (2) can be written as:

$$\ln\left(\frac{Js}{T^2}\right) = \ln(A^*) - \exp\left(-\frac{q\phi_b}{kT}\right) \quad (3)$$

To obtain the saturation current J_s, we can estimate the current based on Fig. 2(b) by linearly extrapolating J to zero voltage. After that, according to Equation 3, the Richardson's plot of the saturation current density was obtained, which is shown in Fig. 2(c). From the linear fit to the plot, the barrier height was calculated to be 1.06 eV, which agrees well with the Schottky barrier height between the β-Ga_2O_3 NM and platinum (Pt) electrode.[26] Finally, the band diagram of flexible β-Ga_2O_3 NM PDs was constructed, as illustrated in Fig. 2(d) and the measured barrier height was large enough for the current rectification in β-Ga_2O_3 NM PDs.

The J-V characteristics of the β-Ga_2O_3 NM PDs were measured both under flat and bending conditions using a 1 mW tunable light source (Horiba, 200 nm ~ 450 nm). As shown in Fig. 3(a), β-Ga_2O_3 NMs PDs exhibited noticeably high photocurrent with the J_{photo}/J_{dark} ratio larger than 10^3 times at -10V at the flat condition. The wavelength-dependent photo responsivity of the device (R_{ph} vs. wavelength) was calculated from the following equation:[25] $R_{ph} = I_{ph} / P_{opt}$, where I_{ph} is the photocurrent and P_{opt} is the power of the incident light. From Fig. 3(b), the peak of the photo responsivity was observed about 0.52 mA/W at 252 nm, which agrees well with the bandgap of β-Ga_2O_3 NMs.[27] Given the performance parameters of the PDs such as the cutoff wavelength of the photodetector (define as the wavelength of the light whose responsivity decrease to 1/e (e ~ 2.718) of the maximum responsivity) at 252 nm and the UV – visible rejection

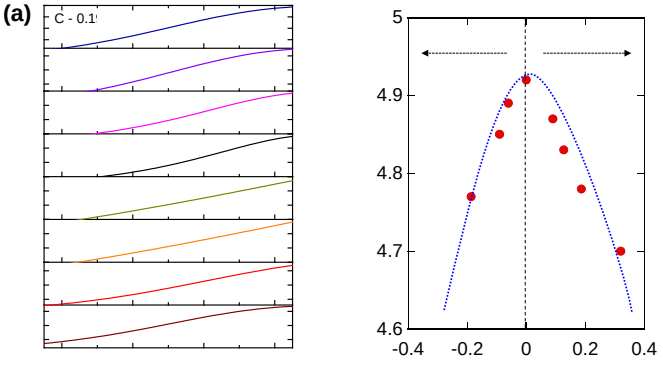

Figure 4. **(a)** Tauc plot for β-Ga_2O_3 NMs under uniaxial tensile and compressive strain. **(b)** Plot of the band gap of β-Ga_2O_3 NMs with respect to uniaxial strain conditions.

ratio (defined as the ratio of the responsivity at 252 nm and 400 nm (R_{252} / R_{400})) of 10^3 times, our β-Ga_2O_3 NMs PDs showed strong solar-blind selectivity and was comparable with the result from rigid forms of β-Ga_2O_3 PDs.[28] Fig. 3(c) shows a single cycle of photoresponse under light illumination to observe the rise time (τ_{rise}, time for the photocurrent to rise from 10 % to 90 %) and the fall time (τ_{fall}, time for the photocurrent to decrease from 90 % to 10 %) which were measured to be 4 sec and 24 sec, respectively, which were related to carrier recombination, generation and the minority carrier lifetime. Compared with the response times during light activation, the relatively slow deactivation response might be attributed to the recombination behavior of the photogenerated carriers in the active region.[29] Optoelectrical properties under different bending conditions were then investigated. In order to study optoelectrical

performance under bending conditions, the device was attached to the convex- and concave-shaped aluminum molds that have different curve radii from 110 to 20 mm which corresponds up to 0.33 % of the uniaxial tensile strain (for the convex mold) and up to 0.19 % of the uniaxial compressive strain (for the concave mold). Fig. 3(d) shows the J–V characteristics of β-Ga_2O_3 NM PDs under 0.33% of the uniaxial tensile strain with UV illumination. The wavelength-dependent photo responsivity of the device under the bending condition is shown in Fig. 3(e). The rejection ratio under the bending condition is slightly decreased to 8×10^{-2} mostly due to a larger photo-current at a visible regime. Interestingly, as the more uniaxial strain was applied, the peak of the photo responsivity gradually shifted to the higher wavelength and reached 260 nm under the highest bending condition (0.33 % of the uniaxial tensile strain). Fig. 3(f) presents the changes in photo responsivity and peak wavelength values under different strain conditions. The highest photo responsivity was also increased from 0.52 A/W at 252 nm to 1.18 A/W at 260 nm under the bending condition. Table 1 shows a comprehensive comparison of our work with some of the representative flexible photodetectors based on wide bandgap single-crystalline semiconductors such as ZnO, GaN, Ga_2O_3 in various forms (nanowires, nanosheets, and thin-films).[4, 30-39]

Interestingly, the peak shifting under the strain condition has never been reported in any other single-crystal semiconductor based photodetectors. To elucidate the reason for this peak shift, the optical property characterization was performed to measure the refractive index (n), extinction coefficient (k), and eventually, bandgap of β-Ga_2O_3 NM under the same strain conditions using a reflection measurement system at the wavelength from 200 nm to 400 nm (Fig. S1). The details of the characterization processes can be found in the supplementary Information. The optical properties of a medium can be described by the complex index of refraction ($N = n - ik$) and the absorption coefficient (α) can be obtained from the extinction coefficient using the following equation: $\alpha(\lambda) = \frac{2\pi k(\lambda)}{\lambda}$.[40, 41] The optical bandgap for the direct electron transition can be calculated using the following formula[42]: $\alpha h\nu = C(h\nu - E_g)^{1/2}$, where $h\nu$ is the photon energy, λ is the wavelength and C is a constant. From the Tauc plot, as shown in Fig. 4(a), the bandgap (E_g) could be estimated by extrapolating the linear sections to the axis of energy ($h\nu$). The optical band gap of β-Ga_2O_3 NM at flat condition is around 4.92 eV, which agrees well with the reported values 4.9 eV of β-Ga_2O_3 NM.[27, 43] Fig. 4(b) and Table S1 summarize the changes of optical bandgap under different strain conditions of β-Ga_2O_3 NM showing the decreasing trend in optical bandgap values from 4.92 eV to 4.75 eV under 0.19% of compressive strain and 4.92 eV to 4.7 eV under 0.33% of tensile strain. Therefore, the reduction in the optical bandgap due to the bending is responsible for the peak shifting from 252 nm to 260 nm.

To further understand the mechanism for the bandgap reduction, we perform the density functional theory (DFT) calculation for strained β-Ga_2O_3 NMs. Although it is difficult to model the realistic material condition in our bending experiment using first-principles methods, we believe that one of the most important consequences of our bending experiment is that it caused a non-uniform strain in the β-Ga_2O_3 NM. The strain variation at the microscopic level may have been much greater than the overall macroscopic strain. This local strain variation then caused both distortion and broadening of both the valence and conduction band edges. This process effectively lowered the conduction band minimum (CBM) and raising the valence band maximum (VBM), thus causing the apparent absorption gap to decrease with both compressive and tensile strain. Therefore, to corroborate the experimental results, we also carried out DFT based first-principles electronic structure calculations of that β-Ga_2O_3 NM under strains, paying particular attention to the shifts in the conduction and valence band edges. All calculations were carried out using pseudopotential plane wave based DFT methods as implemented in the Quantum Espresso package.[44, 45] The Perdew-Burke-Ernzerhof (PBE) functional was used in this work for structural optimizations and electronic structure calculations.[46] Fig. 5(a) shows the three-dimensional crystal structure of β-Ga_2O_3 to indicate the optimized lattice constants for β-Ga_2O_3 are a = 12.333 Å, b = 3.062 Å, and c = 5.838 Å. These values are about 1% larger than the experimental values.[47 48] This is expected since it is known that the PBE functional slightly over-estimates the lattice constant for most materials. In order to investigate the effects on local strain on the band edge states, i.e., CBM and VBM, we carried out constrained structural optimization by applying strain along with one of the lattice direction, while allowing the lattice to relax in other two directions. Fig. 5(b) shows the CBM and VBM states are shifted nearly linearly with applied uniaxial strain with a linear deformation potential $\delta E/(\delta l/l)$ = 14.2 eV and 18.2 eV for the VBM and CBM states, respectively. The local variation of strain (from the mean value) will then cause the band edges to broaden, resulting in narrowing of the bandgap. If we assume a small variation of local strain of ±0.2 %, the corresponding broadening of the VBM state is 14.2 × 0.4% = 0.057 eV, that for the CBM state is 18.2× 0.4% = 0.073 eV. This will give a reduction of the measured band gap of 0.13 eV (0.057 eV + 0.073 eV). Therefore, a small variation in a local stain of ±0.002 (i.e. 0.2 %)

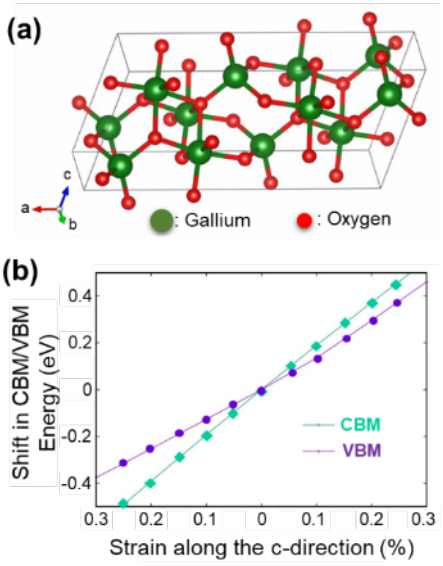

Figure 5. (a) A graphical unit cell of the crystal structure of β-Ga_2O_3. **(b)** Shift in CBM/VBM energy as a function of local uniaxial strain.

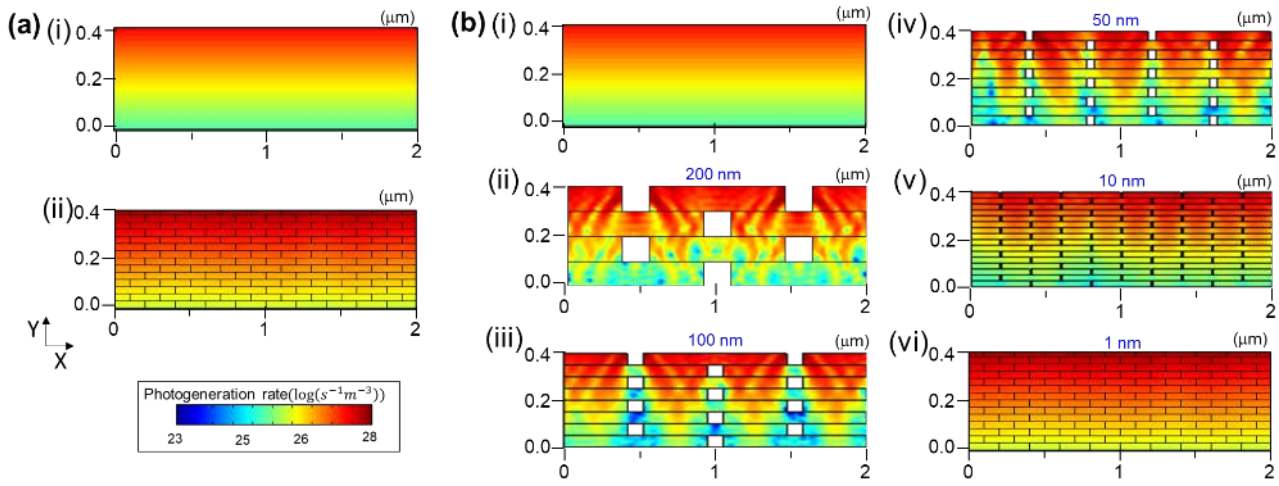

Figure 6. Simulated photogeneration β-Ga_2O_3 NMs on PI substrate under different bending conditions; **(a)** (i) before and (ii) after the formation of nano-cracks in β-Ga_2O_3 NM. **(b)** Simulated photogeneration rate with respect to different gap distances (i) 0 nm, (ii) 200 nm, (iii) 100 nm, (iv) 50 nm, (v) 10 nm, and (vi) 1 nm to show different degree of photogeneration rate in β-Ga_2O_3 NMs.

would be sufficient to cause distortion and broadening of the band edge states to yield a bandgap reduction of about 0.13 eV.

However, while the strain-induced electron transition between neighboring bands explains the shift of the peak photoresponsivity and related bandgap reduction under the strain condition, the higher photo responsivity cannot be explained by the bandgap reduction alone. Therefore, the structure-property study was performed to understand the reason for the higher photo-responsivity under the banding conditions. Firstly, the sidewall of β-Ga_2O_3 NM before and after the bending was investigated using AFM to check any mechanical fractures due to the strain. In order to investigate the structure of β-Ga_2O_3 NM, we prepare the tilted β-Ga_2O_3 NM on PI substrates as shown in Fig. S2(a). The preparation process is similar to the process for the planar type β-Ga_2O_3 NM (as used for β-Ga_2O_3 NM PDs). After spin-coating a 2 um thick SU-8 adhesive layer on top of the PI substrate, another 2 um thick SU-8 layer was formed on half of the top surface, followed by a careful transfer β-Ga_2O_3 NM to obtain a sample with a tilted β-Ga_2O_3 NM. After that, the side surface of β-Ga_2O_3 could be accessed by AFM. Prior to AFM characterization, the sample was bent multiple times (~50 times under 0.5 % of compressive and tensile strain). Fig. S3(a) and (b) compare the sidewall morphologies before and after the bending. While the sidewall morphology of the as-fabricated β-Ga_2O_3 NM sample showed smooth surface roughness (rms roughness: < 1 nm), it became extremely rough after the bending (rms roughness: > 20 nm) with additional fractures. It should be noted that the crystal structure of β-Ga_2O_3 is a monoclinic structure with different bonding strength between longitudinal and horizontal direction, thus, β-Ga_2O_3 has a much weaker bonding force to the longitudinal direction (a-axis in Fig. 5(a)). As a result, β-Ga_2O_3 NMs have a pseudo-layered structure. Therefore, we speculate that the origin of the nano-cracks in strained β-Ga_2O_3 NMs was the monoclinic crystal structure and anisotropic chemical bonds due to an uneven distribution of strain among fractured crystals. To understand the relationship between the nano-cracks in strained β-Ga_2O_3 NMs and its' optoelectrical property, we performed a Multiphysics simulation (COMSOL MULTIPHYSICS) using the mechanical, semiconductor, and optical modules in COMSOL. [49, 50] As shown in Fig. 6(a), the two-dimensional β-Ga_2O_3 NM was created on top of the SU-8 coated PI substrate. To establish a β-Ga_2O_3 layer in the model, the actual material parameters for β-Ga_2O_3 in the model were employed from our experiment data and related literature such as carrier concentration, bandgap, the thickness of β-Ga_2O_3 NM, gaps between nano-cracks in β-Ga_2O_3 NM, and measured optical parameters.[51] In the simulation, a UV light source with a 1 W of power and 250 nm wavelength was illuminated on the top surface of the structure with a 1 V bias across the structure. Fig. 6(a)(i) and (ii) show zoomed-in images of the β-Ga_2O_3 NM at a flat condition and strained condition. We assumed that the β-Ga_2O_3 NM does not have any cracks or delamination at a flat condition, thus it maintains a single body structure. As shown in Fig. 6(a)(i), the photo-generation uniformly occurred across the structure with a rate of about 10^{27} $m^{-3}s^{-1}$ at the top of the β-Ga_2O_3 NM surface and decayed to mid-10^{25} $m^{-3}s^{-1}$ at the bottom of β-Ga_2O_3 NM. On the other hand, as shown in Fig. 6(c)(ii), the fractured β-Ga_2O_3 NM which represents the β-Ga_2O_3 NM under the strain condition exhibited a maximum photo-generation rate of 10^{28} $m^{-3}s^{-1}$ at the top of β-Ga_2O_3 NM surface and 10^{26} $m^{-3}s^{-1}$ at the bottom of β-Ga_2O_3 NM, which is about 10 times larger than as-fabricated β-Ga_2O_3 NMs. The simulation result also agrees with the higher photocurrent under the bending condition compared to the flat condition as discussed in Fig. 3. The simulation suggests that the light shed on the fractured β-Ga_2O_3 NMs can travel much deeper through the nano-cracks, thus increasing the absorption area. Also, illuminated light can stay for a longer time before it decays by reflecting more times inside the β-Ga_2O_3 NMs, which occurred more frequent secondary light absorption. To further understand this optical property, various photogeneration rate simulations with respect to the gap distance ranging from 200 nm to 1 nm were

performed. As shown in Fig. 6(b)(ii), when 200 nm gaps existed in β-Ga_2O_3 NMs, a high-level photogeneration rate occurred at a deeper in β-Ga_2O_3 NM, however, electrical conductivity in β-Ga_2O_3 NM could be severely degraded due to the higher resistance from the existence of nano-gaps. As the distance of nano-gaps became smaller to 1 nm (shown in Fig. 6(b)(vi)), a higher-level of the photogeneration rate occurred at a deeper inside of β-Ga_2O_3 NM, suggesting that the nano-cracks could help β-Ga_2O_3 NM PDs absorb more photons thus enhancing their optoelectrical properties. Another COMSOL MULTIPHYSICS simulation reveals that a stronger strain-induced electric-field is created at edges of fractured β-Ga_2O_3 crystals when β-Ga_2O_3 NM is bent and biased as shown in Fig. S4. It further expands the depletion region in β-Ga_2O_3 NM and as a result, a photogeneration and a current extraction can be increased. Therefore, a strain-induced electric field in β-Ga_2O_3 NM also enhances the light absorption. Furthermore, intrinsic defects, oxygen vacancy in particular, can affect photogeneration in β-Ga_2O_3 NMs. To investigate the evolution of oxygen defects, we prepared two samples: (i) an as-fabricated β-Ga_2O_3 NM and (ii) a fractured β-Ga_2O_3 NM. Both were then inspected using X-ray photoluminescence spectroscopy using an AXIS Ultra DLD XPS (Figure R5). Interestingly, the oxygen/gallium ratio was slightly smaller in the fractured β-Ga_2O_3 NM (1.43 vs. 1.49), indicating oxygen removal. The reduction in oxygen vacancies can enhance photocurrent by the increase hole trapping and rapid transfer of electrons in β-Ga_2O_3 NMs.[6, 52] Nevertheless, the formation of nano-cracks is irreversible, and it degrades the electrical properties of β-Ga_2O_3 NMs until fracturing is complete (nano-cracks are no longer formed). Therefore, a future research topic would determine how the electrical properties could be restored.

Conclusions

In summary, flexible β-Ga_2O_3 NM PDs were successfully fabricated and the electrical and optical properties under bending conditions were characterized. The β-Ga_2O_3 NM PDs showed good solar-blind characteristics with reliable electrical performance under the bending conditions. We observed shifting of the peak wavelength in the photo-current from 252 nm under flat conditions to 260 nm under bending conditions. To investigate the reason for the peak shifting, we performed a structural property analysis using AFM and characterized an optical property of β-Ga_2O_3 NMs, which revealed slight changes in the refractive index and extinction coefficient due to the presence of nano-sized cracks in β-Ga_2O_3 NMs. A Multiphysics structural analysis and a DFT calculation also revealed that the bandgap and nano-gap induced secondary light absorption were responsible for higher photoresponsivity in β-Ga_2O_3 NM PDs. By elucidating the correlation of the structure-property and optoelectrical property in β-Ga_2O_3 NM, our research provides a viable route in the realization of high performance flexible solar-blind photo-detection systems, which is one of the indispensable and important components in the upcoming internet of things era.

Conflicts of interest

There are no conflicts to declare.

Acknowledgements

This work was supported by the National Science Foundation (Grant number: ECCS-1809077) and (Grant number: DMREF-1626967). This work also supported partially by the seed grant by Research and Education in energy, Environment, and Water (RENEW) Institute and Center for Computational Research at the University at Buffalo and Ministry of Education, Singapore, under grant AcRF TIER 1- 2018-T1-002-115 (RG 173/18).

References

1. H. Chen, K. Liu, L. Hu, A. A. Al-Ghamdi and X. Fang, *Materials Today*, 2015, **18**, 493-502.
2. L. Li, E. Auer, M. Liao, X. Fang, T. Zhai, U. K. Gautam, A. Lugstein, Y. Koide, Y. Bando and D. Golberg, *Nanoscale*, 2011, **3**, 1120-1126.
3. Y. Zhao, J. Zhang, D. Jiang, C. Shan, Z. Zhang, B. Yao, D. Zhao and D. Shen, *ACS Applied Materials & Interfaces*, 2009, **1**, 2428-2430.
4. S. Oh, C.-K. Kim and J. Kim, *ACS Photonics*, 2018, **5**, 1123-1128.
5. Y. Qin, L. Li, X. Zhao, G. S. Tompa, H. Dong, G. Jian, Q. He, P. Tan, X. Hou, Z. Zhang, S. Yu, H. Sun, G. Xu, X. Miao, K. Xue, S. Long and M. Liu, *ACS Photonics*, 2020, **7**, 812-820.
6. K. Arora, N. Goel, M. Kumar and M. Kumar, *ACS Photonics*, 2018, **5**, 2391-2401.
7. R. Zou, Z. Zhang, Q. Liu, J. Hu, L. Sang, M. Liao and W. Zhang, *Small*, 2014, **10**, 1848-1856.
8. C. Xie, X.-T. Lu, X.-W. Tong, Z.-X. Zhang, F.-X. Liang, L. Liang, L.-B. Luo and Y.-C. Wu, *Advanced Functional Materials*, 2019, **29**, 1806006.
9. H. Araki, J. Kim, S. Zhang, A. Banks, K. E. Crawford, X. Sheng, P. Gutruf, Y. Shi, R. M. Pielak and J. A. Rogers, *Advanced Functional Materials*, 2017, **27**, 1604465.
10. L. Li, L. Gu, Z. Lou, Z. Fan and G. Shen, *ACS Nano*, 2017, **11**, 4067-4076.
11. X. Xu, J. Chen, S. Cai, Z. Long, Y. Zhang, L. Su, S. He, C. Tang, P. Liu, H. Peng and X. Fang, *Advanced Materials*, 2018, **30**, 1803165.
12. H. Zhou, J.-H. Seo, D. M. Paskiewicz, Y. Zhu, G. K. Celler, P. M. Voyles, W. Zhou, M. G. Lagally and Z. Ma, *Scientific Reports*, 2013, **3**, 1291.
13. J.-H. Seo, E. Swinnich, Y.-Y. Zhang and M. Kim, *Materials Research Letters*, 2020, **8**, 123-144.
14. F. Wang, J.-H. Seo, G. Luo, M. B. Starr, Z. Li, D. Geng, X. Yin, S. Wang, D. G. Fraser, D. Morgan, Z. Ma, X. Wang, *Nature Communications*, 2016, **7** (1), 10444.
15. M. Kim, J.-H. Seo, U. Singisetti and Z. Ma, *Journal of Materials Chemistry C*, 2017, **5**, 8338-8354.
16. M. Kim, J.-H. Seo, Z. Yu, W. Zhou and Z. Ma, *Applied Physics Letters*, 2016, **109**, 051105.
17. J.-H. Seo, K. Zhang, M. Kim, D. Zhao, H. Yang, W. Zhou and Z. Ma, *Advanced Optical Materials*, 2016, **4**, 120-125.
18. J. Seo, J. Li, J. Lee, S. Gong, J. Lin, H. Jiang and Z. Ma, *IEEE Photonics Journal*, 2015, **7**, 1-7.

19. W. S. Hwang, A. Verma, H. Peelaers, V. Protasenko, S. Rouvimov, H. Xing, A. Seabaugh, W. Haensch, C. V. d. Walle, Z. Galazka, M. Albrecht, R. Fornari and D. Jena, *Applied Physics Letters*, 2014, **104**, 203111.
20. X. Yan, I. S. Esqueda, J. Ma, J. Tice and H. Wang, *Applied Physics Letters*, 2018, **112**, 032101.
21. H. Zhou, K. Maize, G. Qiu, A. Shakouri and P. D. Ye, *Applied Physics Letters*, 2017, **111**, 092102.
22. E. Swinnich, M. N. Hasan, K. Zeng, Y. Dove, U. Singisetti, B. Mazumder and J.-H. Seo, *Advanced Electronic Materials*, 2019, **5**.
23. T. Oshima, T. Okuno, N. Arai, N. Suzuki, S. Ohira and S. Fujita, *Applied Physics Express*, 2008, **1**, 011202.
24. M. Kumar, B. Roul, T. N. Bhat, M. K. Rajpalke, A. T. Kalghatgi and S. B. Krupanidhi, *Journal of Nanomaterials*, 2011, **2011**, 189731.
25. S. M. Sze and K. K. Ng, *Physics of semiconductor devices*, John wiley & sons, 2006.
26. Q. He, W. Mu, H. Dong, S. Long, Z. Jia, H. Lv, Q. Liu, M. Tang, X. Tao and M. Liu, *Applied Physics Letters*, 2017, **110**, 093503.
27. E. Swinnich, Y. J. Dave, E. B. Pitman, S. Broderick, B. Mazumder and J.-H. Seo, *Materials Discovery*, 2018, **11**, 1-5.
28. R. Zhuo, D. Wu, Y. Wang, E. Wu, C. Jia, Z. Shi, T. Xu, Y. Tian and X. Li, *Journal of Materials Chemistry C*, 2018, **6**, 10982-10986.
29. J. Park, J.-H. Seo, S.-W. Yeom, C. Yao, V. W. Yang, Z. Cai, Y. M. Jhon and B.-K. Ju, *Advanced Optical Materials*, 2018, **6**, 1701140.
30. S. Wang, H. Sun, Z. Wang, X. Zeng, G. Ungar, D. Guo, J. Shen, P. Li, A. Liu, C. Li and W. Tang, *Journal of Alloys and Compounds*, 2019, **787**, 133-139.
31. B. R. Tak, V. Gupta, A. K. Kapoor, Y.-H. Chu and R. Singh, *ACS Applied Electronic Materials*, 2019, **1**, 2463-2470.
32. N. Kumar, K. Arora and M. Kumar, *Journal of Physics D: Applied Physics*, 2019, **52**, 335103.
33. S. Han, S.-K. Lee, I. Choi, J. Song, C.-R. Lee, K. Kim, M.-Y. Ryu, K.-U. Jeong and J. S. Kim, *ACS Applied Materials & Interfaces*, 2018, **10**, 38173-38182.
34. H. Zhang, X. Dai, N. Guan, A. Messanvi, V. Neplokh, V. Piazza, M. Vallo, C. Bougerol, F. H. Julien, A. Babichev, N. Cavassilas, M. Bescond, F. Michelini, M. Foldyna, E. Gautier, C. Durand, J. Eymery and M. Tchernycheva, *ACS Applied Materials & Interfaces*, 2016, **8**, 26198-26206.
35. Y. Li, Y. Li, J. Chen, Z. Sun, Z. Li, X. Han, P. Li, X. Lin, R. Liu, Y. Ma and W. Huang, *Journal of Materials Chemistry C*, 2018, **6**, 11666-11672.
36. Z. Zheng, L. Gan, J. Zhang, F. Zhuge and T. Zhai, *Advanced Science*, 2017, **4**, 1600316.
37. C. G. Núñez, A. Vilouras, W. T. Navaraj, F. Liu and R. Dahiya, *IEEE Sensors Journal*, 2018, **18**, 7881-7888.
38. J. Zheng, H. Chong, L. Wang, S. Chen, W. Yang, G. Wei and F. Gao, *Journal of Materials Chemistry C*, 2020, **8**, 6072-6078.
39. C.-H. Lin, H.-C. Fu, B. Cheng, M.-L. Tsai, W. Luo, L. Zhou, S.-H. Jang, L. Hu and J.-H. He, *npj 2D Materials and Applications*, 2018, **2**, 23.
40. A. R. Forouhi and I. Bloomer, *Physical Review B*, 1988, **38**, 1865-1874.
41. R. F. Wolffenbuttel, Berlin, Heidelberg, 2001.
42. H. Shen, Y. Yin, K. Tian, K. Baskaran, L. Duan, X. Zhao and A. Tiwari, *Journal of Alloys and Compounds*, 2018, **766**, 601-608.
43. K. Takakura, D. Koga, H. Ohyama, J. M. Rafi, Y. Kayamoto, M. Shibuya, H. Yamamoto and J. Vanhellemont, *Physica B: Condensed Matter*, 2009, **404**, 4854-4857.
44. P. Giannozzi, S. Baroni, N. Bonini, M. Calandra, R. Car, C. Cavazzoni, D. Ceresoli, G. L. Chiarotti, M. Cococcioni, I. Dabo, A. Dal Corso, S. de Gironcoli, S. Fabris, G. Fratesi, R. Gebauer, U. Gerstmann, C. Gougoussis, A. Kokalj, M. Lazzeri, L. Martin-Samos, N. Marzari, F. Mauri, R. Mazzarello, S. Paolini, A. Pasquarello, L. Paulatto, C. Sbraccia, S. Scandolo, G. Sclauzero, A. P. Seitsonen, A. Smogunov, P. Umari and R. M. Wentzcovitch, *J Phys Condens Matter*, 2009, **21**, 395502.
45. P. Giannozzi, O. Andreussi, T. Brumme, O. Bunau, M. B. Nardelli, M. Calandra, R. Car, C. Cavazzoni, D. Ceresoli and M. Cococcioni, *Journal of Physics: Condensed Matter*, 2017, **29**, 465901.
46. J. P. Perdew, K. Burke and M. Ernzerhof, *Physical review letters*, 1996, **77**, 3865.
47. S. Geller, *The Journal of Chemical Physics*, 1960, **33**, 676-684.
48. Y. Yao, S. Okur, L. A. Lyle, G. S. Tompa, T. Salagaj, N. Sbrockey, R. F. Davis and L. M. Porter, *Materials Research Letters*, 2018, **6**, 268-275.
49. T. Anderson, M. Faryad, T. Mackay, A. Lakhtakia and R. Singh, *Journal of Photonics for Energy*, 2016, **6**, 025502.
50. A. Shang and X. Li, *Advanced Materials*, 2017, **29**, 1603492.
51. N. Ma, N. Tanen, A. Verma, Z. Guo, T. Luo, H. Xing and D. Jena, *Applied Physics Letters*, 2016, **109**, 212101.
52. L. X. Qian, H. Y. Liu, H. F. Zhang, Z. H. Wu and W. L. Zhang, *Applied Physics Letters*, 2019, **114**, 113506.

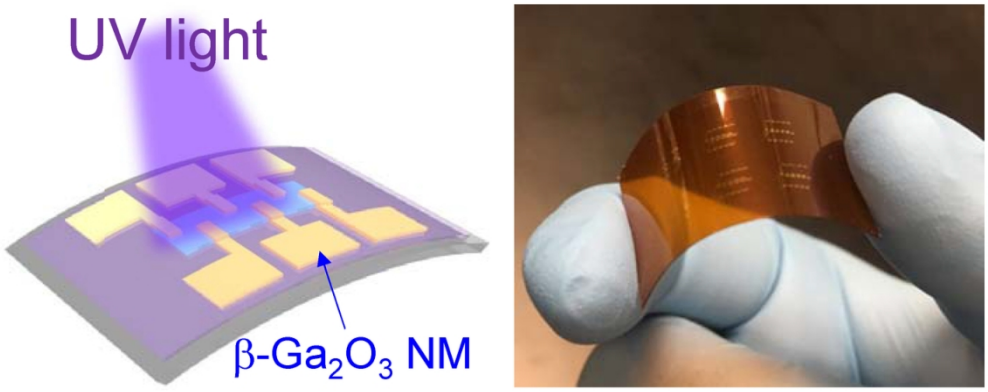

121x49mm (300 x 300 DPI)